Second-Order Topological Photonic Modes in Dipolar Arrays

Yongliang Zhang,[†] Raymond P. H. Wu,[†] Lina Shi,[¶] and Kin Hung Fung[*,†]

†*Department of Applied Physics, The Hong Kong Polytechnic University, Hong Kong, China*

‡*SKLSM, Institute of Semiconductors, Chinese Academy of Sciences, Beijing 100083, China*

¶*Institute of Microelectronics, Chinese Academy of Sciences, Beijing 100029, China*

E-mail: kin-hung.fung@polyu.edu.hk

Abstract

Higher-order topological insulators (HOTIs) are insulators which have novel topological boundary states on the hinges and corners. Herein we generalize them to the photonic HOTIs beyond the conventional scalar coupling by considering the dipolar breathing Kagome lattice. The photonic Kagome lattice supports the out-of-plane and in-plane modes due to the tensorial dipole-dipole interaction. The topological properties of both modes are protected by the generalized chiral symmetry. We show that the topological modes of the out-of-plane mode are similar to the scalar models. Interestingly, in addition to the in-plane corner states in the lower gap protected by the general chiral symmetry, the in-plane mode hosts multiple gapless symmetric and anti-symmetric hinge modes along or transversal to the zigzag and armchair boundaries, which have no counterparts in the scalar models. Our findings demonstrate that the photonic HOTIs have richer physics compared to the scalar counterparts, offer-

ing opportunities for engineering novel electromagnetic applications with topological constraint.

Keywords

Topological Photonics, Topological Insulator, Dipole-dipole interaction, Kagome lattice

1 Introduction

Over the past decade, there have been tremendous parallel advances in the fields of both electronic topological insulators (TIs)[1–3] and engineered bosonic systems of classical waves such as photons[4,5] and acoustics.[6,7] A topological insulator has a band gap in its interior while possing topologically protected conducting states in one dimension lower than the bulk, which are protected by either internal[1–3] or crystalline symmetries.[8] From the perspective of electromagnetic application, the robust boundary modes of photonic topological systems offer great opportunities for optical delay lines,[9] lasers[10] and quantum optics interfaces.[11]

In general, the topology of TIs is characterized by the topological invariant of the Bloch bands, leading to quantized dipolar polarizations.[12] It was recently recognized that there exists higher-order topological insulators (HOTIs) protected by crystalline symmetries,[13–17] manifesting lower order moments bound to the boundaries at least two dimensions lower than the bulk. For instance, several higher-order electronic topological materials with zero dimensional (0D) were predicted,[18–21] and analogue quadrupole insulators corner states were reported in microwave,[22] integrated photonics[23] and phononic metamaterials.[24] Furthermore, the other Wannier-type HOTIs with vanishing Chern number[25–28] have been demonstrated in artificial atomic lattices,[29] acoustic metamaterials[30–32] and 2D photonic crystals.[33–35]

Significant effort has been devoted to the design and realization of HOTIs in diverse physical systems, leading to excellent results and new discoveries. However, existing works of bosonic HOTIs mainly focus on systems with scalar coupling and the findings are similar

to their electronic counterparts. In the present work, we investigate the topological modes of second-order photonic TIs with a focus on the vectorial nature of the electromagnetic wave, which was yet not fully addressed in the recent works on higher-order photonic topological modes of transverse magnetic polarization.[33–35] To be specific, we study the corner states and 1D hinge modes of the photonic breathing Kagome lattice with dipole-dipole interaction. The Kagome lattice is a Wannier-type second-order TI in class AI whose topological index (bulk polarization) is protected by the C_{3v} point group symmetry.[26,27] We notice that the eigen-modes of the dipolar Kagome lattice are decomposed into the out-of-plane and in-plane modes, which furnish different representations of the symmetry group of the effective polarizability matrix. By calculating the eigenmodes of the bulk bands, we show that the symmetry reduction lifts the Dirac degeneracies at higher symmetry points, leading to complete band gaps in both the out-of-plane and in-plane modes. We discuss the existence of the in-gap vectorial corner and hinge states of both modes in the topological phases after band inversion. We find that the topological properties of the out-of-plane mode are similar to the prior works. However, it is interesting that, for the in-plane mode which hosts two complete band gaps, there are several unprecedented transversal and longitudinal hinge modes on both the zigzag and armchair boundaries in different gaps, which are absent in the scalar models. Our results demonstrate that the photonic HOTIs have richer physics compared to the corresponding scalar models, holding opportunities for engineering novel topological states for electromagnetic waves.

2 Theoretical Model

We study the breathing Kagome lattices consisting of spherical subwavelength particles utilizing the eigen-response theory[36,37] which is a semianalytical technique based on the coupled dipole method.[38,39] The geometry of the breathing Kagome lattice is shown in Figure 1a. The lattice is a 2D triangle lattice consisting of three particles per unit cell with unequal intra-cell

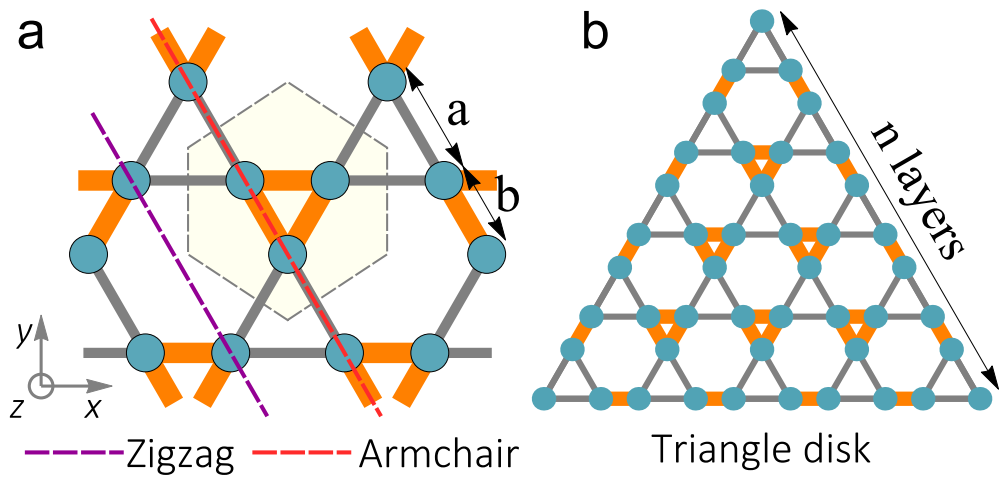

Figure 1: The geometrical structures of (a) the periodic breathing Kagome lattice and (b) the finite triangular disk of the breathing Kagome lattice. The dashed purple and red lines denote the zigzag and armchair boundaries, respectively.

spacing a and inter-cell spacing b. Compared with the standard Kagome lattice, $a > b (a < b)$ corresponds to the expanded (shrunken) unit cell. The lattice primitive vectors are taken to be $\boldsymbol{a}_1 = d\left(\frac{1}{2}\hat{\mathbf{x}} + \frac{\sqrt{3}}{2}\hat{\mathbf{y}}\right)$ and $\boldsymbol{a}_2 = d\left(\frac{1}{2}\hat{\mathbf{x}} - \frac{\sqrt{3}}{2}\hat{\mathbf{y}}\right)$, where $d = a + b$ is the lattice constant. The reciprocal primitive lattice vectors are $\boldsymbol{b}_1 = \frac{4\pi}{\sqrt{3}d}\left(\frac{\sqrt{3}}{2}\hat{\mathbf{x}} - \frac{1}{2}\hat{\mathbf{y}}\right)$ and $\boldsymbol{b}_2 = \frac{4\pi}{\sqrt{3}d}\left(\frac{\sqrt{3}}{2}\hat{\mathbf{x}} + \frac{1}{2}\hat{\mathbf{y}}\right)$. By introducing staggered hopping amplitudes, the rotational C_6 symmetry of the standard Kagome lattice reduces to C_3. Note that the breathing Kagome lattice is a 2D generalization of the 1D Su-Schrieffer-Heeger (SSH) lattice. Previous works have shown that there are three degenerate zero dimension corner states at the zero energy.[26,27] In long wave approximation, the particles are modeled as point dipoles and the lattice sites are assumed to interact with each other by dipole-dipole interaction. The topological phases of dipole-dipole interactions have been studied in several 1D and 2D systems.[36,37,40–44] As mentioned earlier, the eigenmodes for the dipolar Kagome lattice under consideration will decouple to the out-of-plane and in-plane modes, leading to more complex physics than the scalar models.

By using the eigen-response theory, we can analyze the spectral response of dispersive electromagnetic systems with loss and retardation.[36,37] In the dipolar approximation, the subwavelength particles are modeled as point electric dipoles with the dipole moment given

by $\mathbf{p}_n = \boldsymbol{\alpha}_n(\omega)\mathbf{E}_n$. Here $\boldsymbol{\alpha}_n(\omega)$ and $\mathbf{E}_n$ denote the polarizability and electric field at site n. For a cluster of dipolar particles, the total electric field is determined by the incident wave and the radiations from all the particles. Hence, the local electric field at the position of a specific dipole inside the lattice is given by the external incident field and the fields produced by all the other dipoles. In the eigen-response theory, we solve the following non-Hermitian eigenvalue problem based on the self-consistent coupled dipole-dipole interactions[31,38,39]

$$\mathcal{M}(\omega)\mathbf{p} = \lambda(\omega)\mathbf{p}, \tag{1}$$

where $\mathbf{p}(\omega) = [\mathbf{p}_1, \cdots, \mathbf{p}_N]^T$ denotes the dipole moment distribution of a finite system with total N particles, and $\mathcal{M}(\omega, k)$ is the effective polarizability matrix

$$\mathcal{M}_{mn} = \begin{cases} \boldsymbol{\alpha}(\omega)^{-1} & m = n; \\ -\left(k_0^2/\varepsilon_0\right)\mathbb{G}_{mn} & m \neq n, \end{cases} \tag{2}$$

where $\mathbb{G}_{mn}$ is the dyadic Green function which mediates the interaction between dipoles m and n,

$$\mathbb{G}_{mn} = \frac{e^{ikR}}{4\pi R}\left[\left(1 + \frac{ikR - 1}{k^2R^2}\right)\mathbf{I} + \frac{3 - 3ikR - k^2R^2}{k^2R^2}\mathbf{n} \otimes \mathbf{n}\right] \tag{3}$$

with $\mathbf{I}$ is the 3×3 identity matrix, $R = |\mathbf{r}_m - \mathbf{r}_n|$ denotes the distance between two particles, $\mathbf{n} = (\mathbf{r}_m - \mathbf{r}_n)/|\mathbf{r}_m - \mathbf{r}_n|$ the unit vector along the line joining two particles. For spherical particles of radius r_0, the polarizability is given by

$$\boldsymbol{\alpha}(\omega) = \frac{\boldsymbol{\alpha}_0}{1 - ik_0^3\boldsymbol{\alpha}_0/\left(6\pi\varepsilon_0\right)}, \tag{4}$$

where $\boldsymbol{\alpha}_0(\omega) = 3\varepsilon_0 V\left(\varepsilon(\omega) - 1\right)/\left(\varepsilon(\omega) + 2\right)\mathbf{I}$, the second term in denominator represents the radiation correction, $V = 4\pi r_0^3/3$ is the particle's volume and $\varepsilon(\omega)$ is the permittivity of the constituent material. In the present work, we consider the particles made from the low-loss (hexagonal) SiC materials. However, our results can be directly applied to plasmonic

metasurfaces in the visible frequency in spite of the stronger absorption. The permittivity of SiC is modeled by the Lorentz model[45]

$$\varepsilon(\omega) = \varepsilon_\infty \left(1 + \frac{\omega_L^2 - \omega_T^2}{\omega_T^2 - \omega^2 - i\omega\gamma}\right) \tag{5}$$

where $\varepsilon_\infty = 6.7$ is the high frequency limit of the dielectric constant, $\omega_L = 790\,\mathrm{cm}^{-1}$ is the transverse optical phonon frequency, $\omega_L = 966\,\mathrm{cm}^{-1}$ is the longitudinal optical phonon frequency and $\gamma = 2\,\mathrm{cm}^{-1}$ relates to the nonradiative damping rate in the material. Compared with the localized surface plasmon resonance in the visible frequencies supporting by metalic nanoparticles, SiC nanoparticles supports strongly localized phonon polariton resonances in the infrared frequency due to the excitation of longitudinal optical phonons.[45] Here, we choose the radius of the spherical particles to be $r = 100\,\mathrm{nm}$ with the electric dipole resonance at about $928.5\,\mathrm{cm}^{-1}$.

All the spectrum information of a dipolar lattice is contained in the effective polarizability matrix $\mathcal{M}$. In fact, $\mathcal{M}$ plays the same role of the tight binding Hamiltonian in condensed matter physics where the diagonal term is analogous to the on-site energy for the nth particle, while the off-diagonal terms are the hopping terms between arbitrary two sites based on dipole-dipole interaction. In the eigen-response theory, we are interesting to the imaginary part of the eigen-value $\mathrm{Im}\,[\lambda(\omega, k)^{-1}]$ which is proportional to the local density of states of the system.

For a periodic Kagome lattice, we insert the Bloch wave ansatz $\mathbf{p}_{pq} = e^{i\mathbf{k}\cdot\boldsymbol{X}_{pq}}\mathbf{p}$ with $\mathbf{p} = (\mathbf{p}_1, \mathbf{p}_2, \mathbf{p}_3)^T$ and $\boldsymbol{X}_{pq} = p\boldsymbol{a}_1 + q\boldsymbol{a}_2$ to eq 1 to obtain the Bloch eigenvalue problem:

$$\mathcal{M}(\mathbf{k}, \omega)\mathbf{p} = \lambda(\mathbf{k}, \omega)\mathbf{p} \tag{6}$$

where $\mathcal{M}(\omega, k)$ is given by

$$\mathcal{M}_{mn} = \begin{cases} \boldsymbol{\alpha}^{-1} - (k_0^2/\varepsilon_0) \sum\limits_{(p,q)\neq(0,0)} \mathbb{G}_{mn} e^{i\mathbf{k}\cdot\boldsymbol{X}_{pq}}, & m = n; \\ -(k_0^2/\varepsilon_0) \sum\limits_{p,q} \mathbb{G}_{mn} e^{i\mathbf{k}\cdot\boldsymbol{X}_{pq}}, & m \neq n, \end{cases} \tag{7}$$

where $m, n = 1, 2, 3$, $\mathbf{k}$ is the Bloch wave vector, $\mathbb{G}_{mn} = \mathbb{G}(\mathbf{r}_m, \mathbf{r}_n + \boldsymbol{X}_{pq})$ with the integer pair (p, q) denoting the unit cells in the lattice sum.

To get more physical insights, we consider the nearest neighboring coupling approximation by which the corresponding $\mathcal{M}_0(\mathbf{k}, \omega)$ matrix is given by

$$\mathcal{M}_0 = \boldsymbol{\alpha}^{-1} + \mathcal{M}_{\text{hopping}} \tag{8}$$

where

$$\mathcal{M}_{\text{hopping}} = -\frac{k_0^2}{\varepsilon_0} \begin{pmatrix} 0 & m_{12} & m_{13} \\ m_{21} & 0 & m_{23} \\ m_{31} & m_{32} & 0 \end{pmatrix} \tag{9}$$

with

$$m_{12} = \mathbb{G}_{12}(a) + \mathbb{G}_{12}(b) e^{-i\left(k_x + \sqrt{3}k_y\right)a/2}, \tag{10a}$$

$$m_{13} = \mathbb{G}_{13}(a) + \mathbb{G}_{13}(b) e^{-ik_x a}, \tag{10b}$$

$$m_{21} = \mathbb{G}_{12}(a) + \mathbb{G}_{12}(b) e^{i\left(k_x + \sqrt{3}k_y\right)a/2}, \tag{10c}$$

$$m_{23} = \mathbb{G}_{23}(a) + \mathbb{G}_{23}(b) e^{-i\left(k_x - \sqrt{3}k_y\right)a/2}, \tag{10d}$$

$$m_{31} = \mathbb{G}_{13}(a) + \mathbb{G}_{13}(b) e^{ik_x a}, \tag{10e}$$

$$m_{32} = \mathbb{G}_{23}(a) + \mathbb{G}_{23}(b) e^{i\left(k_x - \sqrt{3}k_y\right)a/2}. \tag{10f}$$

Here, the intra-cell hopping $\mathbb{G}_{mn}(a)$ and inter-cell hopping $\mathbb{G}_{mn}(b)$ denote the coupling $\mathbb{G}(\mathbf{r}_m, \mathbf{r}_n)$ between nearest sites m and n with $a(b) = |\mathbf{r}_m - \mathbf{r}_n|$. It is important to note

that the hopping terms are three dimensional complex matrix, representing the tensorial valued coupling in compared with scalar hopping of systems such as the electronic and elastic systems.

In the breathing Kagome lattice the zero frequency corner modes are protected by the generalized chiral symmetry,[30] which is defined by the unitary representation $\Gamma_3 = \mathrm{diag}(1, e^{i2\pi/3}, e^{-i2\pi/3})$. Here, Γ_3 is a direct generalization of the chiral symmetry operator Γ in the SSH model, where $\Gamma H_0 \Gamma^{-1} = -H_0$ with $H_0 = (t_1 + t_2 \cos ka)\sigma_x + t_2 \sin ka \sigma_y$ denoting the SSH Hamiltonian, $\Gamma = \sigma_z$ the chiral operator, and σ_i $(i = x, y, z)$ the Pauli matrix. To include the internal degrees of freedom for the electromagnetic waves, we introduce the generalized chiral symmetry operator

$$\gamma_3 = \Gamma_3 \otimes \mathbf{I}. \tag{11}$$

Under the generalized chiral symmetry γ_3, the $\mathcal{M}_0$ matrix transforms in the following way

$$\gamma_3 \mathcal{M}_0 \gamma_3^{-1} = \mathcal{M}_1, \tag{12a}$$

$$\gamma_3 \mathcal{M}_1 \gamma_3^{-1} = \mathcal{M}_2, \tag{12b}$$

where $\mathcal{M}_1$ and $\mathcal{M}_2$ are isomorphic to $\mathcal{M}_0$, satisfying the constraint

$$\mathcal{M}_0 + \mathcal{M}_1 + \mathcal{M}_2 = 0. \tag{13}$$

Because the chiral symmetry is a consequence of the lattice geometry which is respected by both the out-of-plane and the in-plane modes, it guaranteed the existence of vectorial corner states satisfied with $\sum_{i=1}^{9} \alpha_i^{-1} = 0$. As in the scalar model, the corner states pinned to the zero energy $\alpha_i^{-1} = 0$ satisfied with this constraint automatically, which are confirmed by the following calculations for both the out-of-plane and in-plane modes.

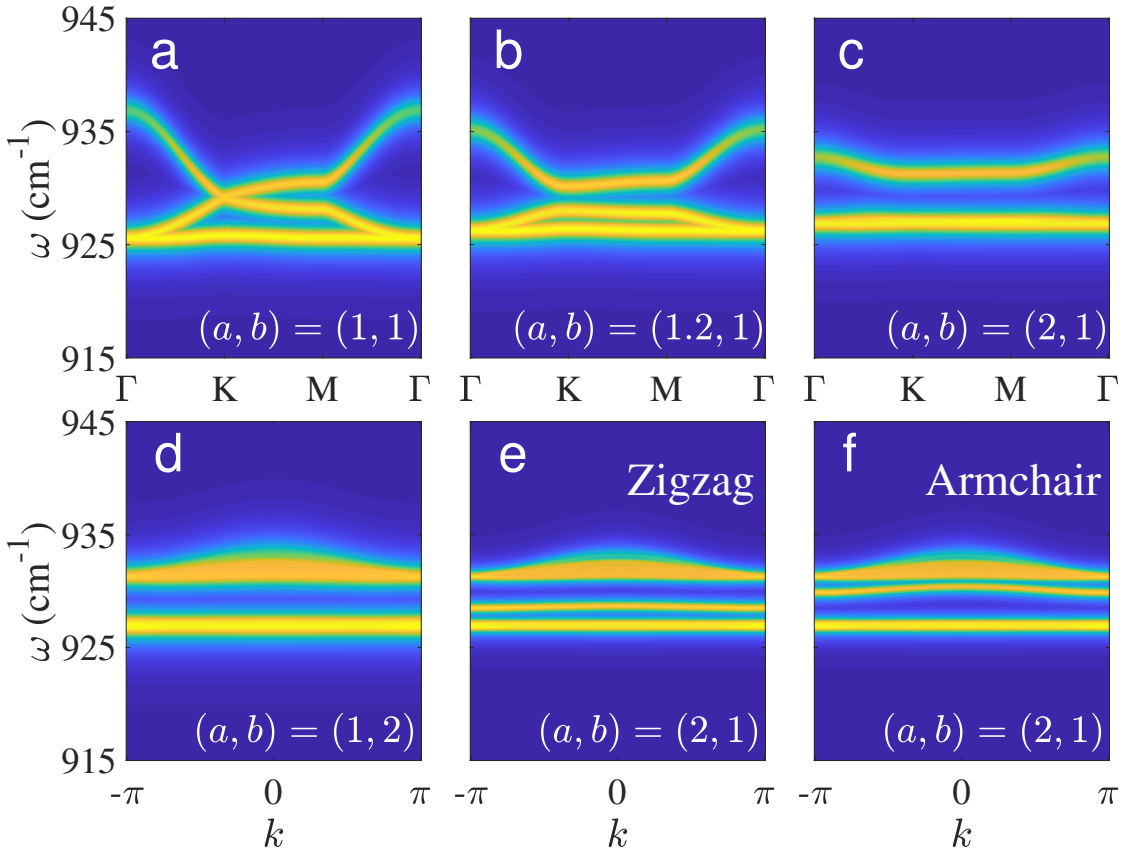

Figure 2: Out-of-plane band structures for (a–c) the bulk breathing Kagome lattices with different hoppings and (d–f) ribbons composed of 1×15 unit cells terminated at the zigzag and armchair boundaries in topologically trivial and nontrivial modes.

3 Out-of-Plane Mode

We first investigate the out-of-plane mode of the breathing Kagome lattice. Because the dipole moment of the out-of-plane mode has only one component along z direction $\mathbf{p} = p\hat{\mathbf{z}}$, it is expected that the feature of the out-of-plane mode are similar to that of the scalar models.[27,30]

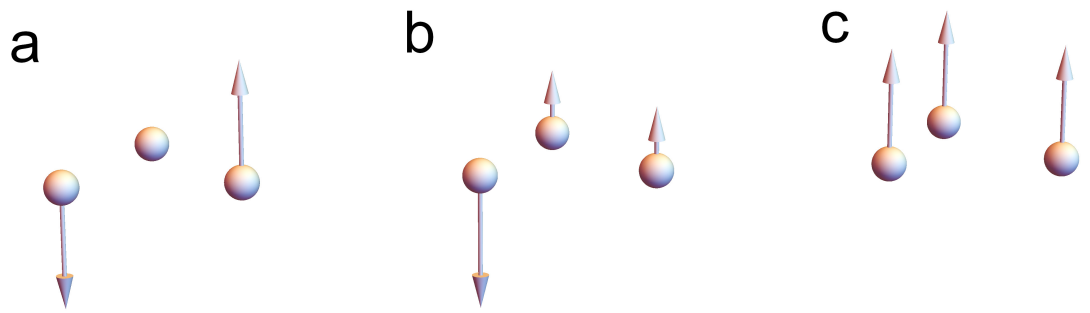

Figure 3: Dipole momentum distributions at M point for the out-plane bands in the metallic phase from the first band to the highest band.

The out-of-plane bulk band structures of the breathing Kagome lattices are shown in Figure 2a–c, where the imaginary parts of the eigen-polarizability $\mathrm{Im}\,[\lambda(\omega, k)^{-1}]$ are presented. To compare with the effect of symmetry reduction due to the staggered hopping, we first consider the band structure of the standard Kagome lattice with $(a = b)$. As shown in Figure 2a, there is a nearly flat band[46] in the lower frequency region and two strongly dispersive bands at higher frequencies are observed. The flat band touches with one of the dispersive bands at Γ point while the upper two bands touch with each other with a Dirac-type degeneracy at K point, which indicates a metallic state. A distinct feature of the dipolar Kagome system is that the flat band locates at the highest frequency region which is in contrast to the scalar systems,[27,30] where the flat band locates at the lowest frequency. These bands originates from the coupling between individual dipolar modes of the particles comprising the trimer constituting the unit cell. The dipole moments in a unit cell for different bands at M point are shown in Figure 3. It is found from Figure 2 that, for the flat band, one of

the dipolar modes interferes destructively in real space due to the lattice symmetry, and is trapped inside the hexagon formed by nearby trimmers. While, the degeneracy is formed between the low frequency in-phase dipolar mode and the high frequency anti-phase dipolar mode on the three particles of the unit cell. By tuning the inter- and intra-cell spacings a and b, the C_6 rotation symmetry is broken to C_3, resulting in a repulsion of the bands at K point, and opening a complete band gap. The symmetry reduction leads to the hybridization and avoided crossing of the formerly degenerated in-phase and anti-phase bands, giving rise to the band inversion. On the other hand, the degeneracy between the lower bands at Γ point are protected and the central band tends to emerge into the lowest one, as can be found in Figure 2b for the case $a = 2b$. Calculations for the case with swapped a and b (not shown) confirms the identical gapped band structure. This result is similar to the SSH model, indicating a topological transition at $a = b$ which corresponds to the band inversion for the two dispersive bands.

Although Chern number vanishes in the Kagome lattice,[25] topological edge modes are excepted to appear in the bulk band gap in the topological phase protected.[26,30] The bulk topology is determined by its polarization, defined as the Brillouin zone average of the Berry connection

$$\mathbf{P} = \frac{1}{2\pi} \iint_{\mathrm{BZ}} \mathrm{Tr}\left[\mathbf{A}(k_x, k_y)\right] d^2k \tag{14}$$

with Berry connection $\mathbf{A} = \langle \mathbf{p} | i\partial_{\mathbf{k}} | \mathbf{p} \rangle$, where $\mathbf{p}$ is the Bloch wave function of the filled bands. Physically, the polarization denotes the center of charge of the Wannier function $\overline{r}_n = \langle w_{n0} | \boldsymbol{r} | w_{n0} \rangle$, where $|w_{n0}\rangle$ is the Wannier function for the n-th band.[12] It can be evaluated at any point in each of the topologically trivial or nontrivial phases because it takes a constant value unless the band inversion occurs.[27] Consider the near field limit, eq 6 for the out-plane mode is given by the real scalar valued hopping $\mathbb{G}_{mn}(r) \to -1/(4\pi k_0^2 r^3), \quad (r = a, b)$. With this, the intra- and inter-cell hoppings become $\kappa = 1/a^3$, $\gamma = 1/b^3$. By which, the nearest neighborring $\mathcal{M}_{\mathrm{hopping}}$ turns out to be Hermitian matrix with elements $m_{12} = \kappa + \gamma e^{-i\left(k_x + \sqrt{3}k_y\right)d/2}, m_{13} = \kappa + \gamma e^{-ik_x d}, m_{23} = \kappa + \gamma e^{i\left(-k_x + \sqrt{3}k_y\right)d/2}$. We note that, in this

case, $\mathcal{M}_{\text{hopping}}$ recovers the tight binding Hamiltonian for scalar waves.[27,30] The out-plane mode can be exactly solved at the limit $\kappa = 0$. As in Ref. 27, the ground state wave function is found to be $\mathbf{p} = \left(1, e^{i(k_x+\sqrt{3}k_y)d/2}, e^{ik_x d}\right)^T$, with which the Berry connection is calculated as $A_x = 1/2$ and $A_y = 1/2\sqrt{3}$. It follows that $p_x = 1/2, p_+ = 0, p_- = 1/2$, and $P_3 = 1/2$. Therefore, the Wannier center exists at the center $(p_x, p_y) = \left(1/2, \sqrt{3}/6\right) a$ of the small triangle. On the contrary, the Wannier center is on the lattice site $(0, 0)$, corresponding to the wave function $\mathbf{p} = (1, 1, 1)^T / \sqrt{3}$ of the trivial phase $\gamma = 0$. Consequently, the mismatch between the Wannier center and the lattice site produces the zero-frequency corner states in the topological phase.

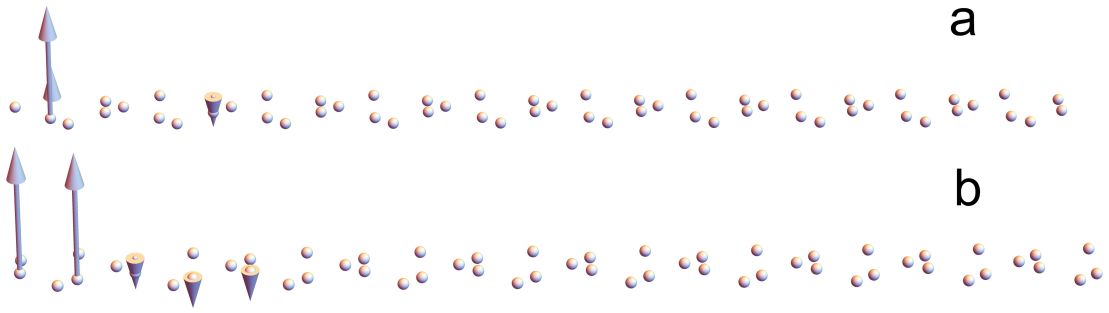

Figure 4: Dipole moments of the edge states on the (a) zigzag and (b) armchair boundaries of the Kagome ribbons in the topological phase.

To confirm the existence of hinge modes, we calculate the band structures of ribbons of the Kagome lattice. In numerical calculations, we set Bloch periodicity across the ribbons. Along the finite direction, we truncate the lattices along the zigzag or armchair boundaries, which are depicted by the dashed lines in Figure 1a. We have examined both situations of topologically trivial ($a < b$) and topologically nontrivial lattices ($a > b$), and found that only in the topological phase the bulk band gap hosts dispersive hinge which strongly localise on the truncated boundaries of the ribbons. The results are shown in Figure 2d–f, where linear ribbons consisting of 1×15 unit cells are calculated. From Figure 2d, the hinge states are absent in the topological trivial case, while Figures 2e and 2f demonstrate the existence of hinge modes in the bulk band gap for each boundary. The corresponding dipole

distributions for the hinge states depicted in Figure 4 show that the lower frequency and upper frequency edge states are bounded at the zigzag and armchair cuts, respectively. We note that the zero frequency is sandwiched between the two branched edge states. It is also worthy mention that the edge states here don't bridge the bulk bands, which is in contrast to Chern insulators.

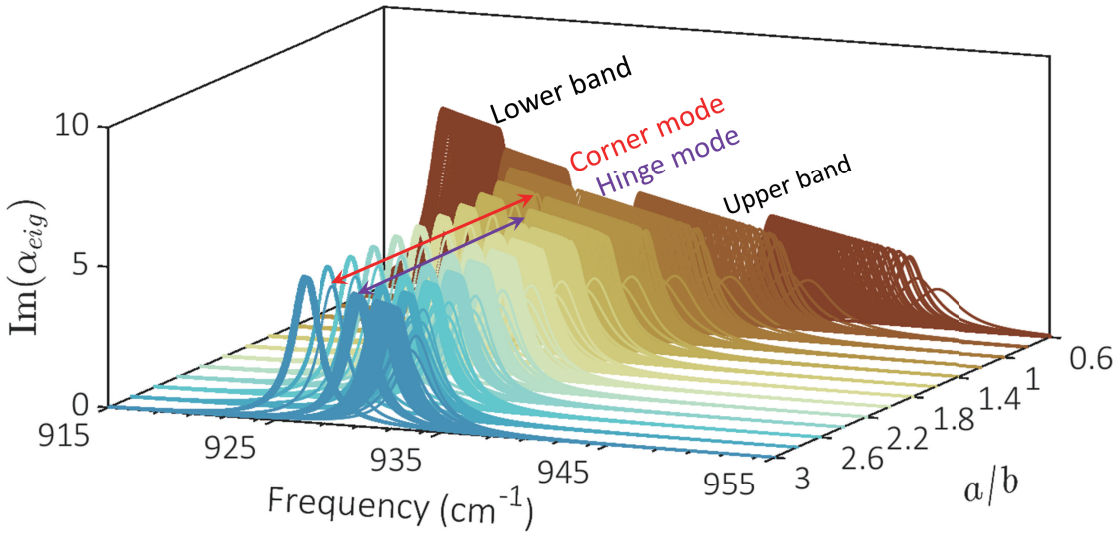

Figure 5: The eigen-polarizability of the out-of-plane modes for finite 21-layer disks of the breathing Kagome lattice with $a/b, (b = 3r_0)$ from 0.6 to 3 with a step 0.2.

Next we investigate the spectral response of finite triangular disks made of the breathing Kagome lattice. We define the size L of the disk by the number of unit cell along one edge. Hence, there are $2L$ particles at each edge and $3L(L+1)/2$ particles in total. The numerical results for a disk of $L = 21$ with different a/b ranging from 0.6 to 3 are shown in Figure 5. It is shown that the band inversion occurs at $a = b$, indicating the closure of the complete band gap. As expect, three nearly degenerate states are found nearby the zero frequency, which are the corner states. Most interestingly, there are $3(N-1)$ discrete gapless states

appearing above the zero frequency in the bulk band gap, which correspond to the hinge mode on the finite sized armchair boundary,[47] as shown in Figure 2f. Both the corner states and the hinge states are only observed the topological non-trivial lattice with $a > b$, they are absent when $a < b$, indicating the topological nature. The distribution of dipole moments for the zero frequency states are depicted in Figure 6a–c. These states well localized at the three corners are linearly combination of the three independent eigen-states with 1/3 charge as previous work,[27] except the fact that the dipole moments of the particles can be parallel or anti-parallel with each other. Figure 6d presents the dipole moment distribution of one of the hinge states inside the bulk gap. It is shown that the response is dominated by the hinges where dipole moments at the sites of neighboring unit cells parallels with each other while antiparallel with the dipoles inside the same unit cell.

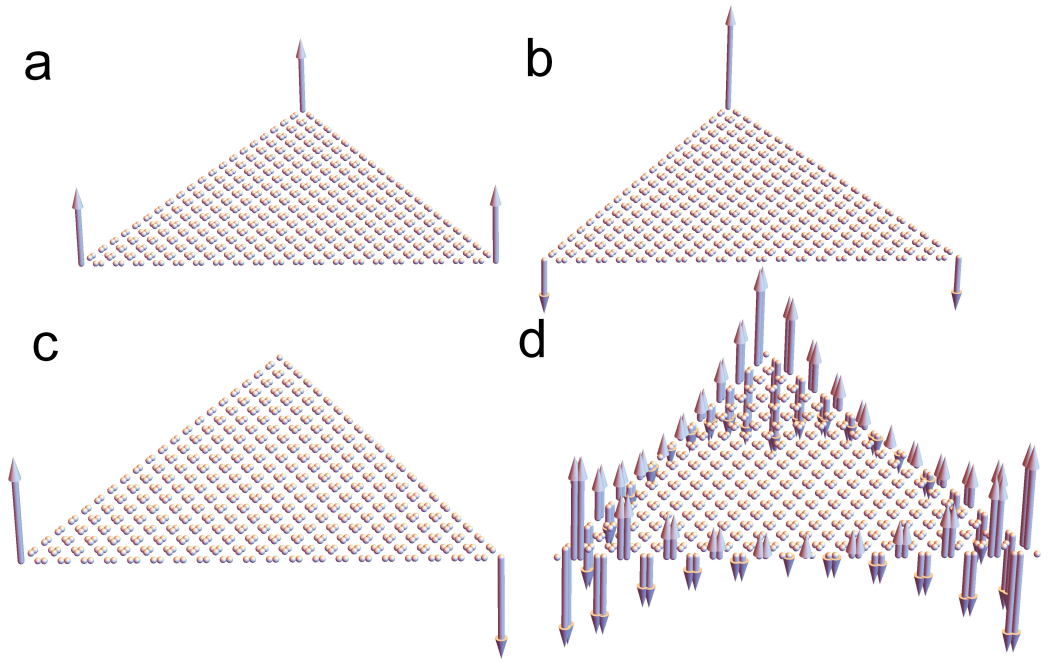

Figure 6: The dipole moment distributions of (a,b,c) the corner states and (d) the hinge state of the triangular disk for the out-of-plane mode in the topological phase.

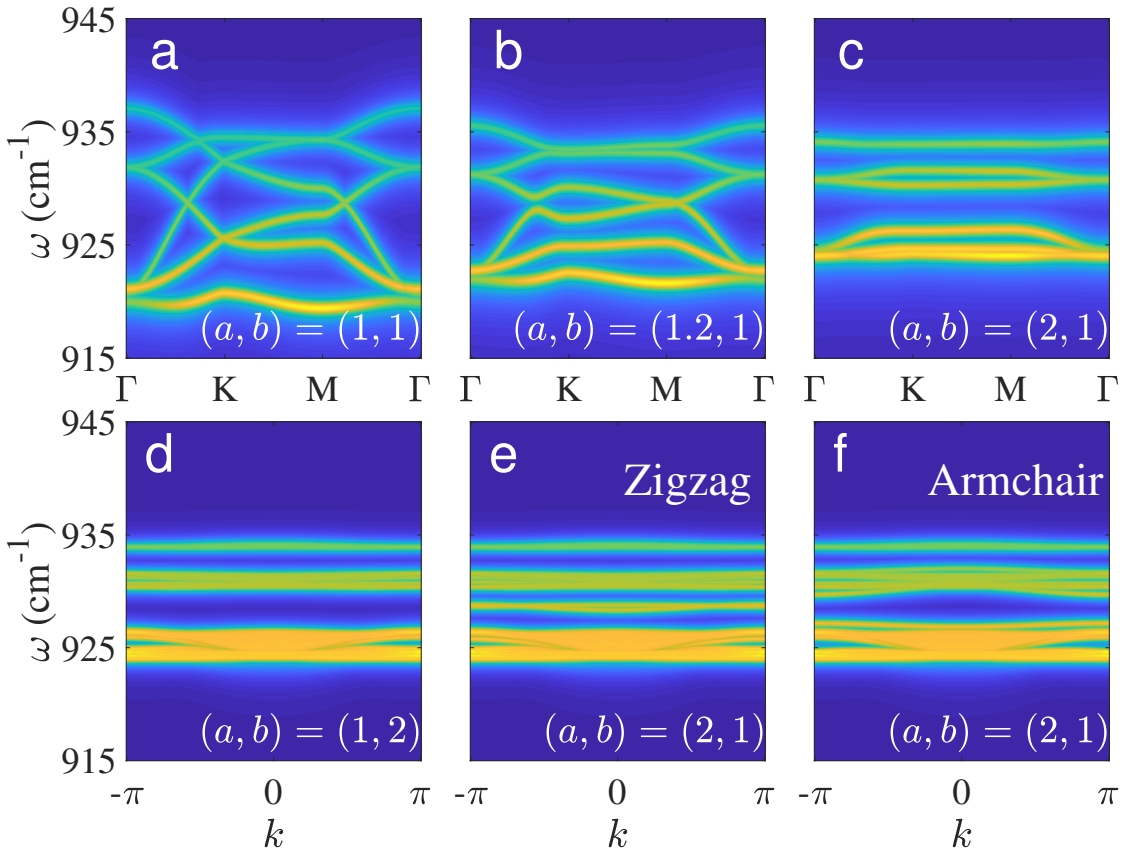

Figure 7: Out-of-plane band structures for (a–c) the bulk breathing Kagome lattices and (d–f) ribbons composed of 1×15 unit cells in the topologically trivial and nontrivial phases.

4 In-Plane Mode

We now study the in-plane mode of the breathing Kagome lattice which is absent in the previous studies. Figure 7a–c presents the bulk band structures for the in-plane mode under study. Because the in-plane dipole moment has two degrees of freedom, there are six bands spanning in the interest frequency region for each structure. As shown in Figure 7a, the standard Kagome lattice ($a = b$) has no complete band gaps. It is found that frequency degeneracies due to band crossing are found at the higher symmetric points K, M and Γ. At K, the central four bands touch linearly at two different frequencies, while the highest two bands are degenerate at M point. Furthermore, the middle two bands and the lower three bands touched at Γ point. The dipole moment distributions at M point for different bands from bottom to top are presented in Figure 8. It is found that the lowest and highest bands have highest symmetries with equal amplitudes; they are rotating and breathing modes, respectively. And the middle four bands consist of one stronger and two weaker dipoles. Specifically, the two weak dipoles point to the center and the other vertex of the triangles for the second and third bands, while the stronger dipole moment is along with y axis. As a comparison, the weaker dipoles points to the upper and lower triangles with anti-parallel components, and the stronger dipole moment point to x axis for the other two bands. Upon symmetry reduction, the degeneracies at K and M points are lifted while the degeneracy at Γ point remains unchanged. It can be seen from Figure 7b for $a = 1.2b$. If the hopping stagger is further increased, as shown in Figure 7c for $a = 2b$, the bands form three disconnected groups among which two complete band gaps emerge. We note that the zero frequency lies in the lower gap. As in the out-of-plane mode, identical bulk band structures are found when the staggered hoppings are interchanged (not shown). Consequently, $a = b$ corresponds to the band inversion point for both bands, indicating a topological transition.

We now consider the Wannier centers for the in-plane mode. For in-plane dipole-dipole coupling, the near-field limit of the Green dyadic $\mathbb{G}_{mn}(R) \to 1/(4\pi k^2 R^3)\,(-1 + 3\mathbf{n} \otimes \mathbf{n})$. By

which, the real tensor valued hopping matrix $\mathcal{M}_{\text{hopping}}$ is given by

$$
\begin{aligned}
m_{12} &= \boldsymbol{\kappa}_{12} + \boldsymbol{\gamma}_{12} e^{-i\left(k_x/2+\sqrt{3}k_y/2\right)d}, && \text{(15a)}\\
m_{13} &= \boldsymbol{\kappa}_{13} + \boldsymbol{\gamma}_{13} e^{-ik_x d}, && \text{(15b)}\\
m_{23} &= \boldsymbol{\kappa}_{23} + \boldsymbol{\gamma}_{23} e^{i\left(-k_x/2+\sqrt{3}k_y/2\right)d}, && \text{(15c)}
\end{aligned}
$$

where we have defined

$$
\begin{aligned}
\boldsymbol{\kappa}_{12} &= \frac{1}{a^3}\begin{pmatrix} -1/4 & 3\sqrt{3}/4 \\ 3\sqrt{3}/4 & 5/4 \end{pmatrix}, && \text{(16a)}\\
\boldsymbol{\kappa}_{13} &= \frac{1}{a^3}\begin{pmatrix} 2 & 0 \\ 0 & -1 \end{pmatrix}, && \text{(16b)}\\
\boldsymbol{\kappa}_{23} &= \frac{1}{a^3}\begin{pmatrix} -1/4 & -3\sqrt{3}/4 \\ -3\sqrt{3}/4 & 5/4 \end{pmatrix}. && \text{(16c)}
\end{aligned}
$$

The inter-cell $\boldsymbol{\gamma}_{mn}$ are obtained by replacing a with b in the above expressions. With the above matrix valued hopping, it is very difficult to analytically evaluate the Wannier center. However,the Wannier center for the topologically trivial case can be found to locate at the lattice center $(0,0)$ trivially since both $\mathcal{M}$ and the eigen-vectors don't depend on $\boldsymbol{k}$ in the limit $\boldsymbol{\gamma}_{mn} \to 0$. For the topological phase, numerical calculation shows the Wannier center locates at the triangle center $\left(1/2, \sqrt{3}/6\right) a$ as previously. So that the mismatch of the Wannier centers indicates the difference between the topological trivial and non-trivial phases, giving rise to the topological states for the in-plane mode.

We now consider the hinge states on the boundaries of Kagome ribbons. It is expected that the in-plane hinge modes are more complicated than the out-of-plane mode because of the complex bulk band structures, as show in Figure 7a–c. The band structure for the topologically trivial ribbon is shown in Figure 7d, where two complete band gaps are observed

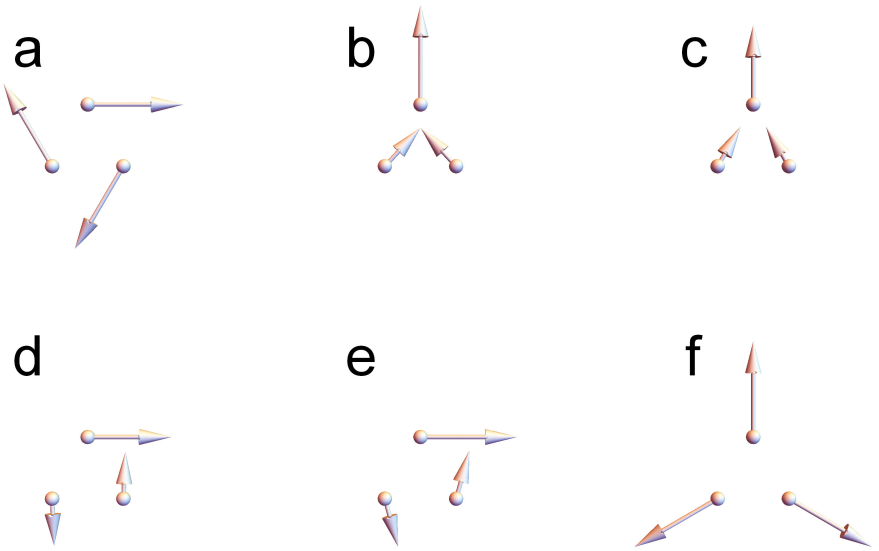

Figure 8: Dipole momentum distributions of the bulk bands at M point for the in-plane topological mode (a/b=2) from the first band to the highest band.

clearly. Figures 7e and f present the band structures for ribbons with zigzag and armchair cuts in the topological phase, respectively. By comparing with the topological trivial phase, we find that the zigzag boundary has two hinge modes residing inside the lower gap, which touch with each other at Γ point. The dipole moment distributions shown in Figure 9 demonstrates that both modes are well localized on the ribbon's boundaries, and the dipole moment directions are aligned and vertical with the ribbons, respectively. For the armchair boundary shown in Figure 7f, it is very interesting that both bulk band gaps host hinge modes, which is different from the zigzag boundary where two hinge modes are found in the lower gap. To be specific, there are two dispersive hinge modes in the lower gap and one hinge mode in the upper gap for the zigzag boundary. In Figure 9b, we plot the dipole moments for the three hinge states from bottom to top. It is shown that the edge state in the upper gap is a longitudinal mode with antisymmetric dipole moments inside the unit cell. For the two lower hinge states, the dipole moments are perpendicular to the ribbon, and represent the symmetric and antisymmetric modes, respectively. Because the antisymmetric mode has lower energy, the frequency of the antisymmetric mode is lower than the symmetric one.

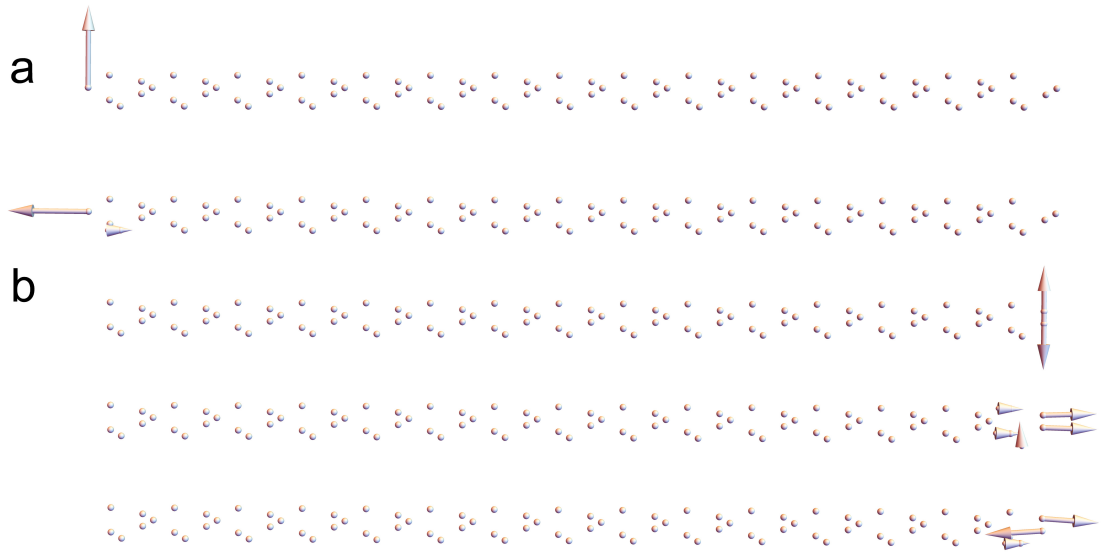

Figure 9: Dipole moments of the edge states of the in-plane mode on (a) the zigzag and (b) the armchair boundaries of the Kagome ribbons in the topological phase.

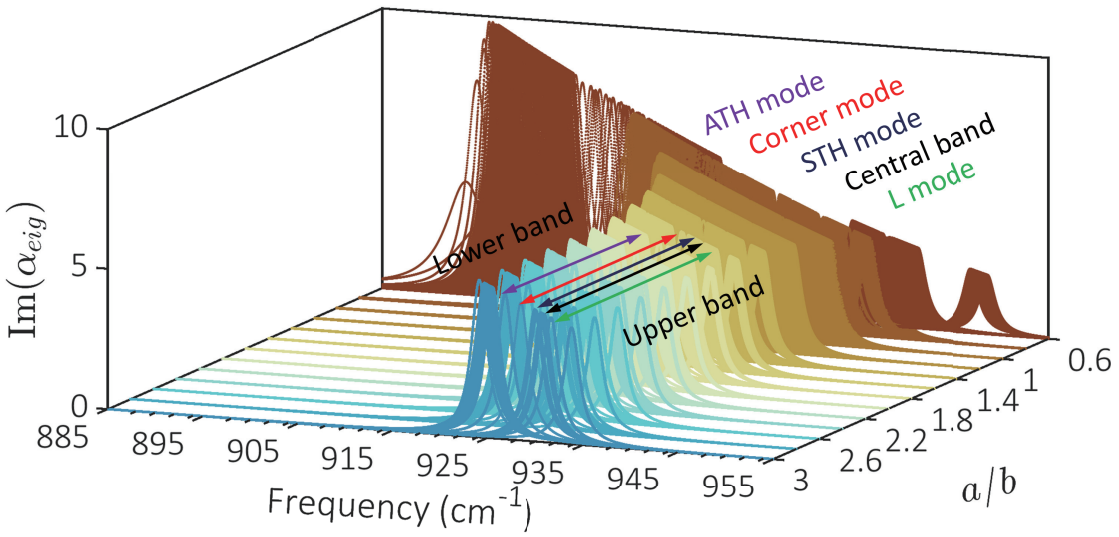

Figure 10: Dependence of the imaginary part of the eigen-polarizability of the in-plane mode on the distance aspect ratio a/b. Here, ATH, STH and L modes denote the anti-symmetric transverse mode, the symmetric transverse mode and the longitudinal mode, respectively.

As in the out-of-plane mode, we also calculate the responses of the finite triangular disks for different parameters. The effective eigen-polarizabilities of the finite triangular disks are presented in Figure 10. It is found that six nearly degenerate states retain near the zero mode frequency in the lower gap of the topological nontrivial phase ($a/b > 1$). The corresponding dipole moment distributions shown in Figure 11a–f are linearly combinations of states localized at the corners. We want to point out that the direction of the dipole moment on each of the vertexes is either perpendicular or aligned with the corresponding line connecting the vertex and the center of the disk. These corner states are linearly combinations of the associated dipoles on the corner sites. Besides the corner states, there are three dispersive bands resided in both the bulk band gaps of the topological phase. Two hinge modes are found in the lower gap in which the zero modes are sandwiched. While, a single hinge mode is found in the upper gap, which is in agreement with the result shown in Figure 7f. Specifically, there are $3(L-1)$ states below the zero frequency and $2L$ states above the zero frequency. Form Figures 11g,h, the dipoles of the two modes are the anti-symmetric and symmetric modes perpendicular to the boundaries. Finally, there are $3(L-1)$ longitudinal states in the upper band gap, whose dipole moments are aligned with the directions of the boundary [See Figure 11i].

5 Conclusion

In summary, we have investigated the second-order vectorial topological modes on the photonic breathing Kagome lattice with dipole-dipole interactions. We show that symmetry breaking lifts the degeneracies at higher frequency points, leading to complete band gaps for both the out-of-plane and in-plane modes. In both modes, vectorial corner states are found near zero frequencies in the band gaps. For the out-of-plane mode, two gapless hinge modes are observed on the zigzag and armchair boundaries, respectively. For the in-plane mode, we show that there are two hinge states which are aligned and perpendicular to the

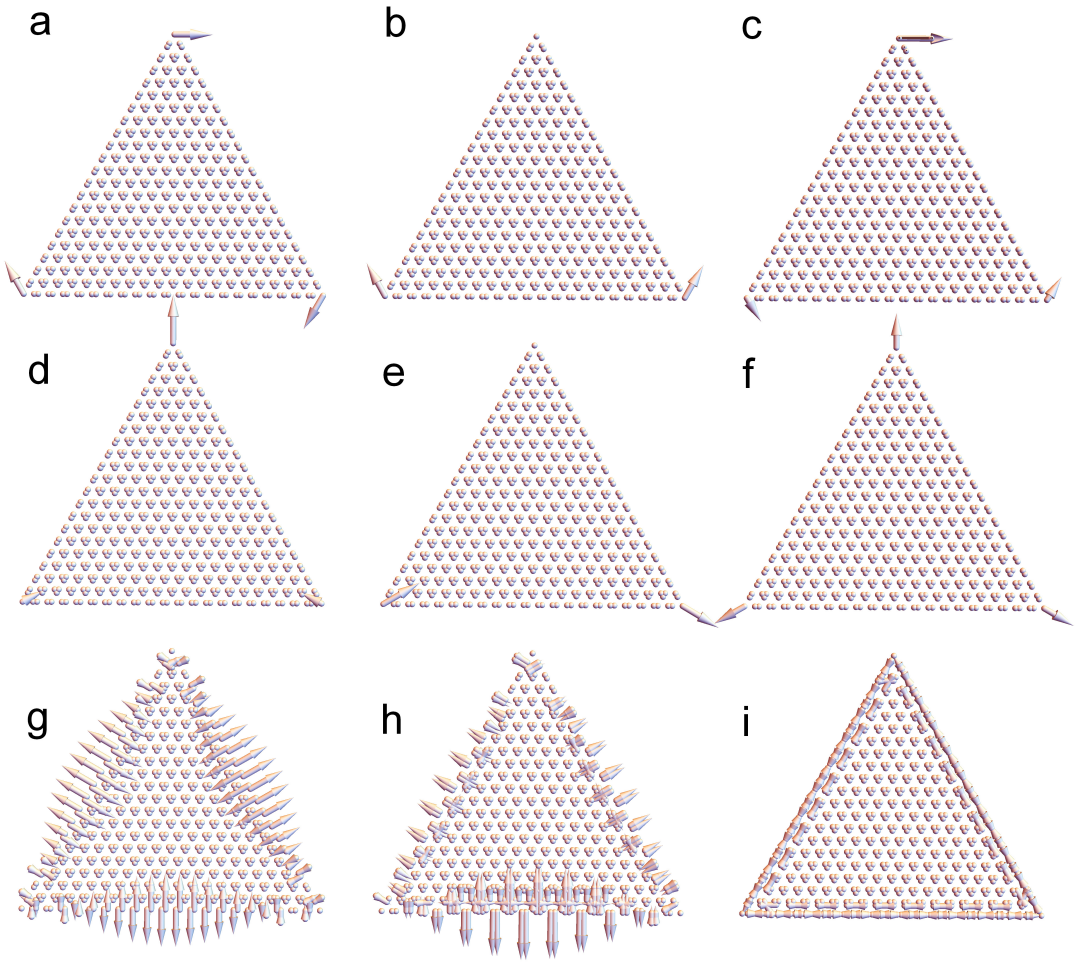

Figure 11: Dipole distributions of the (a–f) corner states, (g,h) the antisymmetric and symmetric transversal hinge modes, and (i) the longitudinal hinge mode supported by the Kagome triangle in the topological phase.

zigzag boundary in the lower gap. Meanwhile, three hinge states, one longitudinal and two transversal modes with symmetric and anti-symmetric dipoles are found on the armchair boundary, which are absent in the scalar model. Our work reveals the intriguing difference between the electromagnetic fields and other scalar models, which can also be applied to the other non-Hermitian systems such as plasmonic metasurfaces in the optical frequencies.

Acknowledgement

We thank Kai Fung Lee, Wang Tat Yau, Wai Chun Wong and Lau Ting Wai for helpful discussions. This work is supported by Collaborative Research Fund from the Hong Kong Research Grant Council (grant No. C6013-18G) and the National Natural Science Foundation of China under Grant No. 61875225.

References

(1) Hasan, M. Z.; Kane, C. L. Colloquium: Topological insulators. *Rev. Mod. Phys.* **2010**, *82*, 3045–3067.

(2) Qi, X.-L.; Zhang, S.-C. Topological insulators and superconductors. *Rev. Mod. Phys.* **2011**, *83*, 1057–1110.

(3) Chiu, C.-K.; Teo, J. C. Y.; Schnyder, A. P.; Ryu, S. Classification of topological quantum matter with symmetries. *Rev. Mod. Phys.* **2016**, *88*, 035005.

(4) Lu, L.; Joannopoulos, J. D.; Soljačić, M. Topological photonics. *Nat. Photon.* **2014**, *8*, 821.

(5) Ozawa, T.; Price, H. M.; Amo, A.; Goldman, N.; Hafezi, M.; Lu, L.; Rechtsman, M. C.; Schuster, D.; Simon, J.; Zilberberg, O.; Carusotto, I. Topological photonics. *Rev. Mod. Phys.* **2019**, *91*, 015006.

(6) Süsstrunk, R.; Huber, S. D. Classification of topological phonons in linear mechanical metamaterials. *Proc. Natl. Acad. Scr. U. S. A.* **2016**, *113*, E4767–E4775.

(7) Zhang, X.; Xiao, M.; Cheng, Y.; Lu, M.-H.; Christensen, J. Topological sound. *Commun. Phys.* **2018**, *1*, 1–13.

(8) Fu, L. Topological Crystalline Insulators. *Phys. Rev. Lett.* **2011**, *106*, 106802.

(9) Mittal, S.; Fan, J.; Faez, S.; Migdall, A.; Taylor, J. M.; Hafezi, M. Topologically Robust Transport of Photons in a Synthetic Gauge Field. *Phys. Rev. Lett.* **2014**, *113*, 087403.

(10) Bandres, M. A.; Wittek, S.; Harari, G.; Parto, M.; Ren, J.; Segev, M.; Christodoulides, D. N.; Khajavikhan, M. Topological insulator laser: Experiments. *Science* **2018**, *359*.

(11) Barik, S.; Karasahin, A.; Flower, C.; Cai, T.; Miyake, H.; DeGottardi, W.; Hafezi, M.; Waks, E. A topological quantum optics interface. *Science* **2018**, *359*, 666–668.

(12) Vanderbilt, D. *Berry Phases in Electronic Structure Theory: Electric Polarization, Orbital Magnetization and Topological Insulators*; Cambridge University Press, 2018.

(13) Benalcazar, W. A.; Bernevig, B. A.; Hughes, T. L. Quantized electric multipole insulators. *Science* **2017**, *357*, 61–66.

(14) Benalcazar, W. A.; Bernevig, B. A.; Hughes, T. L. Electric multipole moments, topological multipole moment pumping, and chiral hinge states in crystalline insulators. *Phys. Rev. B* **2017**, *96*, 245115.

(15) Bradlyn, B.; Elcoro, L.; Cano, J.; Vergniory, M.; Wang, Z.; Felser, C.; Aroyo, M.; Bernevig, B. A. Topological quantum chemistry. *Nature* **2017**, *547*, 298.

(16) Khalaf, E. Higher-order topological insulators and superconductors protected by inversion symmetry. *Phys. Rev. B* **2018**, *97*, 205136.

(17) van Miert, G.; Ortix, C. Higher-order topological insulators protected by inversion and rotoinversion symmetries. *Phys. Rev. B* **2018**, *98*, 081110.

(18) Schindler, F.; Wang, Z.; Vergniory, M. G.; Cook, A. M.; Murani, A.; Sengupta, S.; Kasumov, A. Y.; Deblock, R.; Jeon, S.; Drozdov, I., et al. Higher-order topology in bismuth. *Nat. Phys.* **2018**, *14*, 918.

(19) Schindler, F.; Cook, A. M.; Vergniory, M. G.; Wang, Z.; Parkin, S. S. P.; Bernevig, B. A.; Neupert, T. Higher-order topological insulators. *Scr. Adv.* **2018**, *4*.

(20) Yue, C.; Xu, Y.; Song, Z.; Weng, H.; Lu, Y.-M.; Fang, C.; Dai, X. Symmetry-enforced chiral hinge states and surface quantum anomalous Hall effect in the magnetic axion insulator Bi 2–x Sm x Se 3. *Nat. Phys.* **2019**, *15*, 577.

(21) Xu, Y.; Song, Z.; Wang, Z.; Weng, H.; Dai, X. Higher-Order Topology of the Axion Insulator $EuIn_2As_2$. *Phys. Rev. Lett.* **2019**, *122*, 256402.

(22) Peterson, C. W.; Benalcazar, W. A.; Hughes, T. L.; Bahl, G. A quantized microwave quadrupole insulator with topologically protected corner states. *Nature* **2018**, *555*, 346.

(23) Mittal, S.; Orre, V. V.; Zhu, G.; Gorlach, M. A.; Poddubny, A.; Hafezi, M. Photonic quadrupole topological phases. *Nat. Photon.* **2019**, 1.

(24) Serra-Garcia, M.; Peri, V.; Süsstrunk, R.; Bilal, O. R.; Larsen, T.; Villanueva, L. G.; Huber, S. D. Observation of a phononic quadrupole topological insulator. *Nature* **2018**, *555*, 342.

(25) Liu, F.; Wakabayashi, K. Novel Topological Phase with a Zero Berry Curvature. *Phys. Rev. Lett.* **2017**, *118*, 076803.

(26) Benalcazar, W. A.; Li, T.; Hughes, T. L. Quantization of fractional corner charge in C_n-symmetric higher-order topological crystalline insulators. *Phys. Rev. B* **2019**, *99*, 245151.

(27) Ezawa, M. Higher-Order Topological Insulators and Semimetals on the Breathing Kagome and Pyrochlore Lattices. *Phys. Rev. Lett.* **2018**, *120*, 026801.

(28) Kunst, F. K.; van Miert, G.; Bergholtz, E. J. Lattice models with exactly solvable topological hinge and corner states. *Phys. Rev. B* **2018**, *97*, 241405.

(29) Kempkes, S.; Slot, M.; van den Broeke, J.; Capiod, P.; Benalcazar, W.; Vanmaekelbergh, D.; Bercioux, D.; Swart, I.; Smith, C. M. Robust zero-energy modes in an electronic higher-order topological insulator. *Nat. Mater.* **2019**, 1–6.

(30) Ni, X.; Weiner, M.; Alù, A.; Khanikaev, A. B. Observation of higher-order topological acoustic states protected by generalized chiral symmetry. *Nat. Mater.* **2019**, *18*, 113.

(31) Xue, H.; Yang, Y.; Gao, F.; Chong, Y.; Zhang, B. Acoustic higher-order topological insulator on a kagome lattice. *Nat. Mater.* **2019**, *18*, 108.

(32) Xue, H.; Yang, Y.; Liu, G.; Gao, F.; Chong, Y.; Zhang, B. Realization of an Acoustic Third-Order Topological Insulator. *Phys. Rev. Lett.* **2019**, *122*, 244301.

(33) Xie, B.-Y.; Su, G.-X.; Wang, H.-F.; Su, H.; Shen, X.-P.; Zhan, P.; Lu, M.-H.; Wang, Z.-L.; Chen, Y.-F. Visualization of Higher-Order Topological Insulating Phases in Two-Dimensional Dielectric Photonic Crystals. *Phys. Rev. Lett.* **2019**, *122*, 233903.

(34) Chen, X.-D.; Deng, W.-M.; Shi, F.-L.; Zhao, F.-L.; Chen, M.; Dong, J.-W. Direct Observation of Corner States in Second-Order Topological Photonic Crystal Slabs. *Phys. Rev. Lett.* **2019**, *122*, 233902.

(35) Wong, S.; Saba, M.; Hess, O.; Oh, S. S. Gapless Unidirectional Photonic Transport Using All-Dielectric Kagome Lattices. 2019.

(36) Zhang, Y.-L.; Wu, R. P. H.; Kumar, A.; Si, T.; Fung, K. H. Nonsymmorphic symmetry-protected topological modes in plasmonic nanoribbon lattices. *Phys. Rev. B* **2018**, *97*, 144203.

(37) Wu, R. P. H.; Zhang, Y.; Lee, K. F.; Wang, J.; Yu, S. F.; Fung, K. H. Dynamic long range interaction induced topological edge modes in dispersive gyromagnetic lattices. *Phys. Rev. B* **2019**, *99*, 214433.

(38) Markel, V. Coupled-dipole Approach to Scattering of Light from a One-dimensional Periodic Dipole Structure. *J. Mod. Opt.* **1993**, *40*, 2281–2291.

(39) Ross, M. B.; Mirkin, C. A.; Schatz, G. C. Optical Properties of One-, Two-, and Three-Dimensional Arrays of Plasmonic Nanostructures. *J. Phys. Chem. C* **2016**, *120*, 816–830.

(40) Wang, L.; Zhang, R.-Y.; Xiao, M.; Han, D.; Chan, C. T.; Wen, W. The existence of topological edge states in honeycomb plasmonic lattices. *New Journal of Physics* **2016**, *18*, 103029.

(41) Downing, C. A.; Weick, G. Topological collective plasmons in bipartite chains of metallic nanoparticles. *Phys. Rev. B* **2017**, *95*, 125426.

(42) Pocock, S. R.; Xiao, X.; Huidobro, P. A.; Giannini, V. Topological Plasmonic Chain with Retardation and Radiative Effects. *ACS Photon.* **2018**, *5*, 2271–2279.

(43) Proctor, M.; Craster, R. V.; Maier, S. A.; Giannini, V.; Huidobro, P. A. Exciting Pseudospin-Dependent Edge States in Plasmonic Metasurfaces. *ACS Photon.* **2019**, *6*, 2985–2995.

(44) Proctor, M.; Huidobro, P. A.; Maier, S. A.; Craster, R. V.; Makwana, M. P. Manipulating Topological Valley Modes in Plasmonic Metasurfaces. 2019.

(45) Wang, B. X.; Zhao, C. Y. Topological phonon polaritons in one-dimensional non-Hermitian silicon carbide nanoparticle chains. *Phys. Rev. B* **2018**, *98*, 165435.

(46) Nakata, Y.; Okada, T.; Nakanishi, T.; Kitano, M. Observation of flat band for terahertz spoof plasmons in a metallic kagomé lattice. *Phys. Rev. B* **2012**, *85*, 205128.

(47) Weber, W. H.; Ford, G. W. Propagation of optical excitations by dipolar interactions in metal nanoparticle chains. *Phys. Rev. B* **2004**, *70*, 125429.

Graphical TOC Entry